Supporting Information

Cobalt single-atom catalyst with ultralow metal loading for activation of peroxymonosulfate to generate singlet oxygen with almost 100% selectivity

Yuanzhe Zhao[a,b], Xiuheng Wang[a,b,*]

[a]State Key Laboratory of Urban Water Resource and Environment, Harbin Institute of Technology, Harbin 150090, China;

[b]School of Environment, Harbin Institute of Technology, Harbin 150090, China

*Corresponding author.

E-mail address: xiuheng@hit.edu.cn.

This file includes:

Texts: S1-4

Figures: S1-20

Tables: S1-5

SI References

Text S1

Characterizations. The powder X-ray diffraction (XRD) patterns were characterized using a SmartLab-SE diffractometer (Japan) with Cu Kα radiation over a range from 10 to 60°. The surface properties of catalysts were measured by a Fourier transform infrared spectroscopy (FTIR, Nicolet iS20, Thermo Fisher Scientific Co., USA). A Raman spectrometer (Horiba LabRAM HR Evolution, Japan) was used to measure the structure defect of catalysts. The magnetic characteristics of catalysts were analyzed by a vibrating-sample magnetometer (VSM, LakeShore7404, USA). X-ray photoelectron spectroscopy (XPS) analysis was conducted on an Escalab 250Xi (Thermo Scientific K-Alpha, USA) equipped with an Al Kα X-ray source. Elemental compositions of catalysts were detected by inductively coupled plasma-atomic emission spectrometry (ICP-OES, Agilent 5800, USA). The Brunauer-Emmett-Teller (BET) specific surface area and pore size distribution of catalysts were measured by N_2 adsorption-desorption using a Micromeritics ASAP 2460 instrument (USA) at -196 °C. The scanning electron microscope (SEM) images of catalysts were collected using ZEISS Gemini 300 (Germany) equipped with energy dispersive spectrometer (EDS). Transmission electron microscopy (TEM) images were obtained on a JEM-200CX electron microscope (Japan) operated at 200 kV. The images of isolated single Co atoms were obtained using an aberration-corrected high-angle annular dark-field scanning transmission electron microscopy (AC-HAADF-STEM, JEOL-ARM200 F, Japan) with an operating voltage of 200 kV. K-edge X-ray adsorption fine structure (XAFS) tests including X-ray absorption near edge structure (XANES) and extended X-ray absorption fine structure (EXAFS) measurements at the Co K edge were carried out on Shenzhen HuaSuan Technology Co., Ltd with stored electron energy of 2.2 GeV using a transmission mode. Electrochemical tests including electrochemical impedance spectroscopy (EIS) Nyquist plots, Tafel plots, *I-t* curves, linear sweep voltammetry (LSV) curves and cyclic voltammetry (CV) curves were conducted in an electrochemistry workstation (CHI760E, China) to investigate the electrochemical characteristics of catalysts and electron transfer in PMS activation.

Text S2

Experimental Procedure. Degradation experiments were performed in a 250 mL conical flask containing 100 mL of TC solution (10 mg/L) with an initial solution pH of 6.95 at ambient temperature. Typically, 15 mg of the catalyst was dispersed into TC solution completely, and the reaction was triggered after adding PMS. 2 mL of reaction solution was withdrawn and immediately quenched with 1 mL of $Na_2S_2O_3$ solution (0.1mol/L) at specified time intervals. After filtered through a 220-nm Millipore film, residual TC was determined. In the control experiment of PMS activation by the homogeneous cobalt catalyst, the cobalt content of the Co^{2+}/PMS system was the same as the Co-N-C/PMS system, which was adjusted by adding 0.2 mg of $CoCl_2 \cdot 6H_2O$ to the reaction system. For recycling experiments, catalysts were filtered after each run, thoroughly rinsed with pure water, dried under vacuum, and then reused in the subsequent cycle. To verify the practical application of the catalytic system, some key factors including initial solution pH (adjusted by 0.1 M HCl or NaOH solution), different pollutants (BPA, CPL, CBZ, SD, and RhB), coexisting inorganic anions (Cl^-, SO_4^{2-}, NO_3^-, HCO_3^-, PO_4^{2-} and HCO_3^-) and HA were explored. In quenching experiments, certain amount of scavengers such as MeOH (k_1(•OH, MeOH)=9.7×10^8 M^{-1} s^{-1}, k_2($SO_4^{\bullet-}$, MeOH)=2.5×10^7 M^{-1} s^{-1}), TBA (k (•OH, TBA)=3.8-7.6$\times10^8$ M^{-1} s^{-1}), and p-BQ (k($O_2^{\bullet-}$, p-BQ)=2.9×10^9 M^{-1} s^{-1}),[1] which were calibrated by the molar ratio with PMS to distinguish the participation of •OH, $SO_4^{\bullet-}$ and $O_2^{\bullet-}$, while furfuryl alcohol (FFA) and DMSO were applied to scavenge $^1O_2$ (k=1.2×10^8 M^{-1} s^{-1}) [2] and high-valent Co species.[3] In addition, for exploring the effect of dissolved oxygen on TC degradation, the reaction solutions were bubbled by argon (200 mL min^{-1}) for 30 min before the reaction starts. Most degradation experiments were conducted in triplicates and the average data with their standard deviations were presented. Tap water was collected from municipal water supply, while the Songhua River water was located as in (45°48′N, 126°39′E), and concentrated TC was added to the above water reaching 10 mg/L.

The steady-state concentration and contribution of radicals are detected by probe methods, and the detailed procedures are as follows:

•OH and $SO_4^{\bullet-}$ concentration measurement. Benzoic acid (BA) was used as a molecular probe to detect •OH and $SO_4^{\bullet-}$ concentration because of the high second-order reaction rate constants between BA and •OH (4.2×10^9 $M^{-1}s^{-1}$) and $SO_4^{\bullet-}$ (1.2×10^9 $M^{-1}s^{-1}$).[4, 5] The N_2 aeration tube was immersed in 100.0 mL of BA aqueous solution (0.1 mM BA) before the reaction, and O_2 in the solution was excluded. Then, 0.15 g/L catalyst and 0.5 mM PMS were added. After a defined time interval, a 1 mL sample was taken out from the quartz reactor using a syringe and filtered through a 0.22 μm PTFE filter, and quenched with MeOH immediately. The •OH and $SO_4^{\bullet-}$ concentration was calculated by the loss quantitation of BA. The concentration of residual BA was measured by HPLC at 225 nm, the mobile phase was methanol/2%-phosphoric acid (45/55, v/v), and the flow rate was 0.2 mL/min.

$O_2^{\bullet-}$ concentration measurement. Nitrotetrazolium blue chloride (NBT) was used as the molecular probe of $O_2^{\bullet-}$.[6] The aeration tube was immersed in 100.0 mL of NBT aqueous solution (0.1 mM) before the reaction, and oxygen content in the solution was controlled by aeration with air and pure oxygen. Add 0.15 g/L catalyst and 0.5 mM PMS in the NBT solution to initiate the reaction. At predetermined time intervals, 1 mL of sample was taken and filtered through a 0.22 μm nitrocellulose membrane. The yellow NBT was reduced to blue formazan by $O_2^{\bullet-}$, and the concentration change of NBT was measured at 259 nm with UV-vis spectrophotometer. The $O_2^{\bullet-}$ concentration was calculated by the loss quantitation of NBT.

$^1O_2$ concentration measurement. Using FFA as an indicator of $^1O_2$.[7] The aeration tube was immersed in 100.0 mL of FFA ethanol solution (0.1 mM) before the reaction, and oxygen content in the solution was controlled by aeration with air and pure oxygen. Add 0.15 g/L catalyst and 0.5 mM PMS to initiate the reaction. At predetermined time intervals, 1 mL of sample was taken and filtered through a 0.22 μm nitrocellulose membrane, and the concentration change of FFA was measured by HPLC at 219 nm with the mobile phase of methanol/water (50/50, v/v), and the flow rate was 1.0 mL/min. The steady-state concentration of $^1O_2$ was calculated by dividing the slope of the straight line fitted from $\ln FFA(C_0/C)$ versus reaction time by the second-order reaction rate constant between $^1O_2$ and FFA (1.2×10^8 M^{-1} s^{-1}).

Text S3

Analytic Methods. The concentration of residual PMS during reaction was detected using a modified potassium iodide method.[8] Firstly, 10 mM KI stock solution was prepared by dissolving 0.166 g of KI and 0.04 g of $NaHCO_3$ in 100 mL of deionized water. Secondly, mix 0.1 mL of the water sample with 4.9 mL of the KI stock solution. After allowing the reaction to proceed for 5 min, the concentration of PMS was finally obtained by detecting the absorbance at a wavelength of 352 nm with UV-vis spectrophotometer. TC and RhB concentration were determined by monitoring the absorbance at 357 nm and 554 nm with a UV-vis spectrophotometer, while BPA, CPL, CBZ, and SD concentration were analyzed via high-performance liquid chromatography (HPLC, Agilent, 1260-Infinity, USA) equipped with an Agilent HC-C18 column (150×4.6 mm, 5μm) and the column temperature was set at 30 ◦C, and the detailed information is provided in Table S1. The mineralization of TC in catalytic reactions was determined by a total organic carbon (TOC) analyzer (Multi N/C 3100, Germany). Intermediates from TC degradation was analyzed by an ultra-high performance liquid chromatography-mass spectrometry (UPLC-MS) system (Dionex Ultimate 3000, USA) equipped with an Eclipse Plus C18 column (100 mm × 4.6 mm). The mobile phase was a 0.1% (by volume) aqueous formic acid (A, 80%) and acetonitrile (B, 20%) solution with a flow rate of 0.35 mL/min, and column temperature was set at 30 ℃. The leaching of cobalt ions from Co-N-C after the reaction was quantified using ICP-OES. Electron paramagnetic resonance (EPR, Bruker ESR5000, Germany) tests were carried out to detect reactive oxygen species during PMS activation, using DMPO and TEMP as spin-trapping agents, respectively. The generation of $^1O_2$ was detected by a Singlet Oxygen Sensor Green (SOSG)-based method. First, 100 μg of SOSG was dissolved in 300 μL deoxygenated methanol to obtain a SOSG solution (500 μM). Catalysts (5 mg) and 10 mL of deionized water were added into a 25 mL glass beaker under stirring. Then, 40 μL of SOSG solution was added to the beaker; 20 μL of 0.1 M PMS was added to initiate the reaction. After 1 min, 200 μL of the sample was withdrawn and diluted to 5 mL. Then, the obtained sample was immediately filtered using a 0.22 μm PTFE syringe filter. Finally, the sample was assessed by fluorescence spectrometer. The excitation wavelength was 450 nm and the emission wavelength was 530 nm. XAFS data were processed according to the standard procedures using the Athena module implemented in the IFEFFIT software packages. EXAFS spectra were obtained by subtracting the post-edge background from the overall absorption and then normalizing with respect to the edge-jump step, subsequently, the $\chi(k)$ data of were Fourier transformed to real (R) space using a hanning window (dk = 1.0 $Å^{-1}$) to separate the EXAFS contributions from different coordination shells. To obtain the quantitative structural parameters around central atoms, least-squares curve parameter fitting was performed using the ARTEMIS module of IFEFFIT software packages.[9, 10]

Text S4

DFT Calculations. DFT calculations were performed by the Vienna ab initio simulation package (VASP). All the spin-polarized calculations are performed in the framework of the density functional theory with the projector augmented plane-wave method, as implemented in the Vienna ab initio simulation package [11]. The nuclei-electron and the electron exchange correlation interactions were described by the projector augmented wave (PAW) potentials [12] and the generalized gradient approximation (GGA) [13] with the Perdew-Burke Ernzerh of (PBE) [14] functional, respective. The cut-off energy for plane wave is set to 400 eV. The energy criterion is set to 10^{-6} eV in iterative solution of the Kohn-Sham equation. A vacuum layer of 15 Å is added perpendicular to the sheet to avoid artificial interaction between periodic images. The Brillouin zone integration is performed using a 2x2x1 k-mesh. All the structures are relaxed until the residual forces on the atoms have declined to less than 0.03 eV/Å.

Supplementary Figures

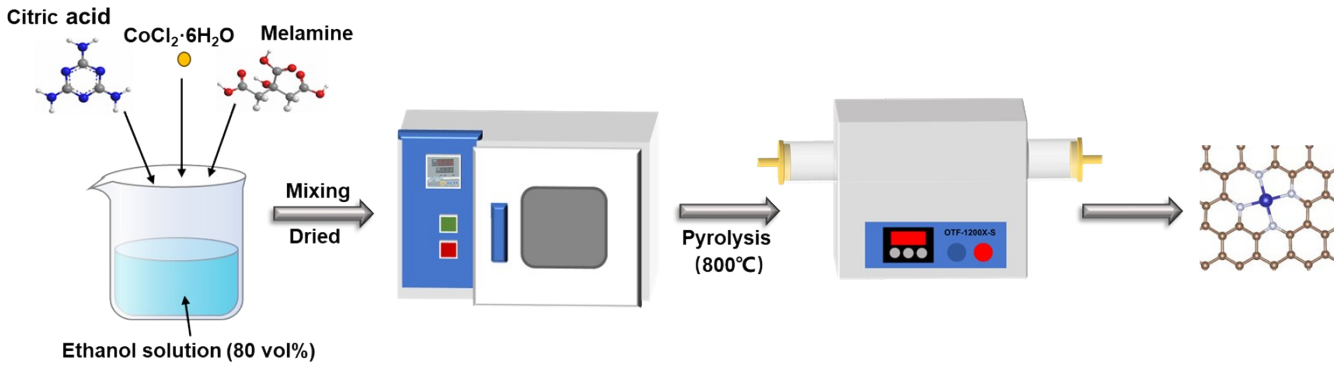

Figure S1. Synthesis of Co-N-C.

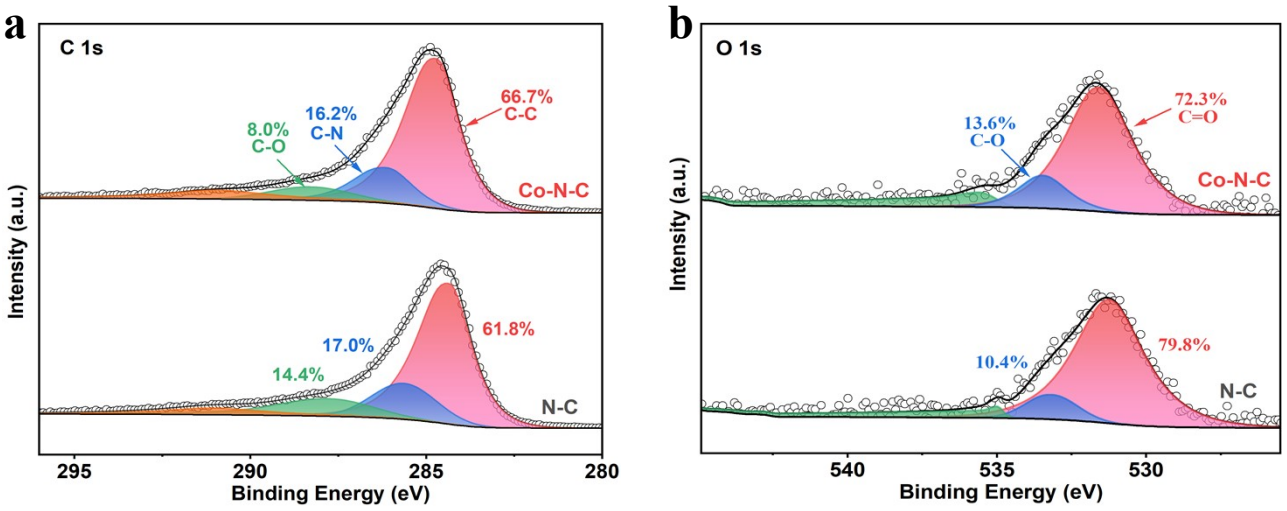

Figure S2. XPS spectra of N-C and Co-N-C: (a) C 1s and (b) O 1s.

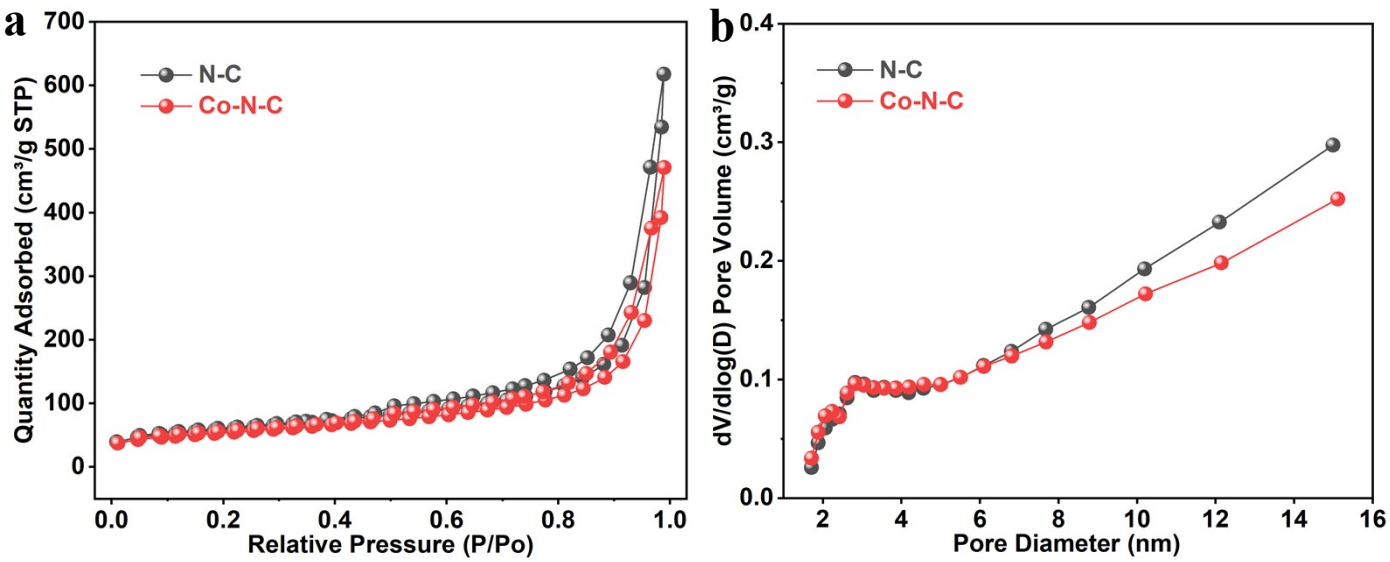

Figure S3. (a) N_2 adsorption-desorption isotherms of N-C and Co-N-C and (b) the corresponding pore size distribution.

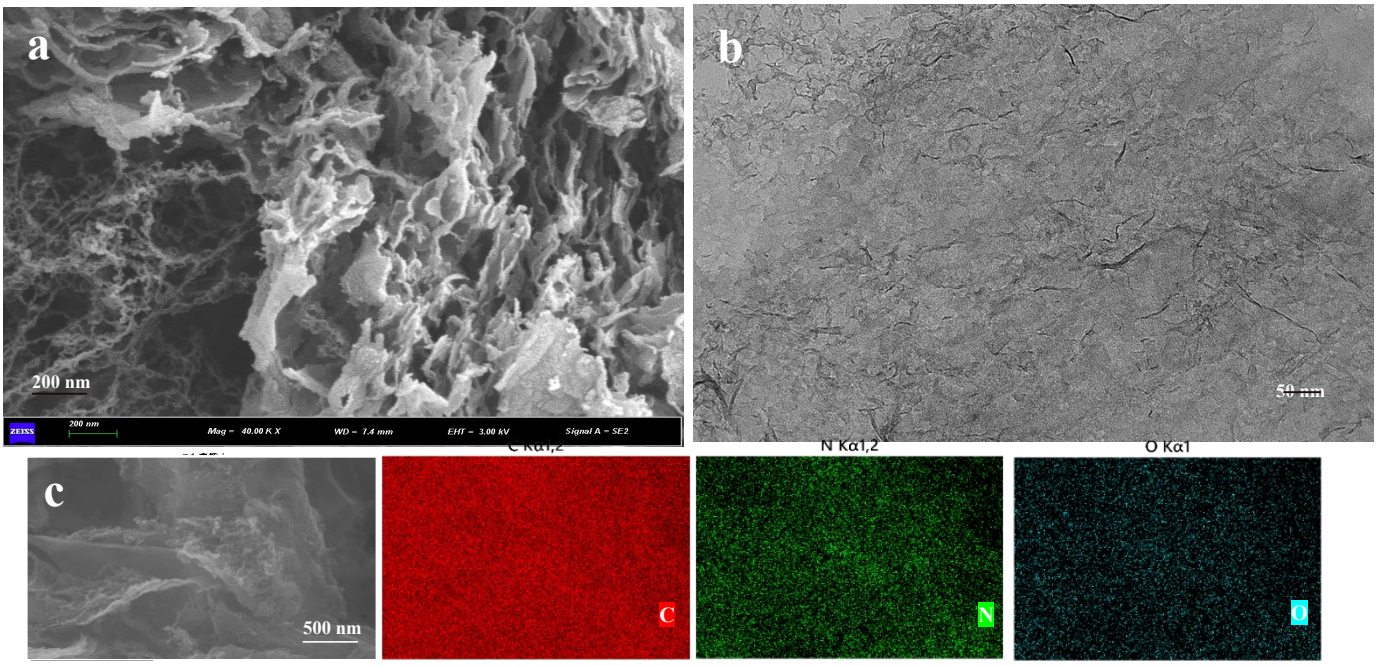

Figure S4. (a) SEM, (b) TEM and (c) EDX images of N-C.

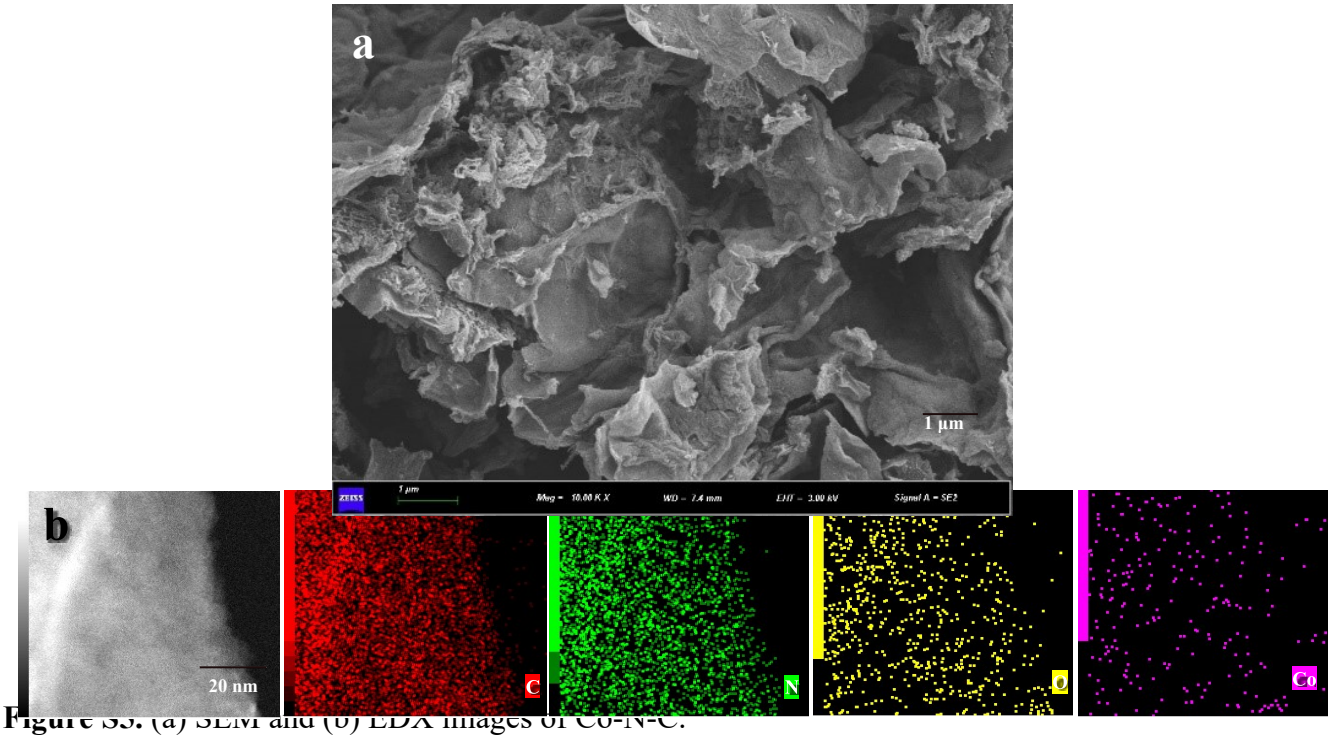

Figure S3. (a) SEM and (b) EDX images of Co-N-C.

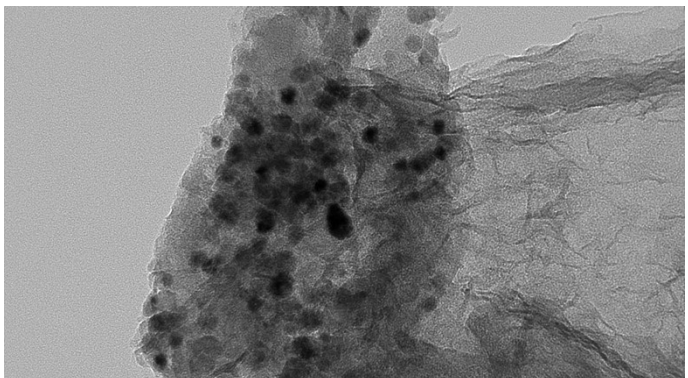

Figure S6. TEM image of CoNP-N-C.

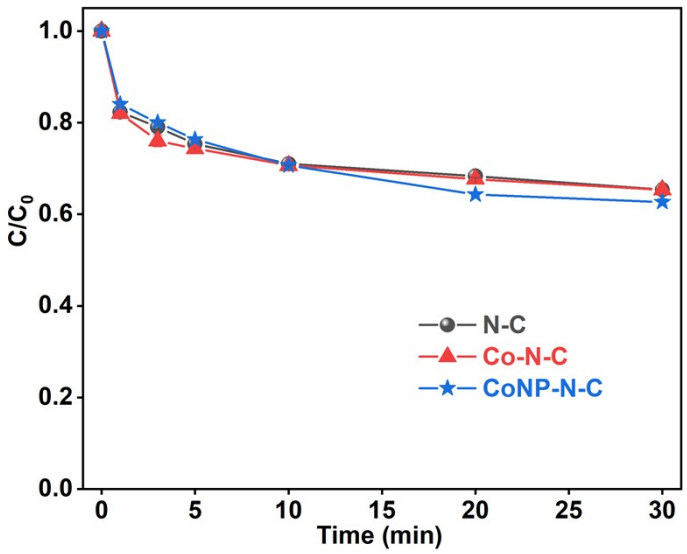

Figure S7. Adsorption of TC by catalysts. Experimental conditions: $[TC]_0$ = 10 mg L^{-1}, $[catalyst]_0$ = 0.15 g L^{-1}, temperature = 25 °C.

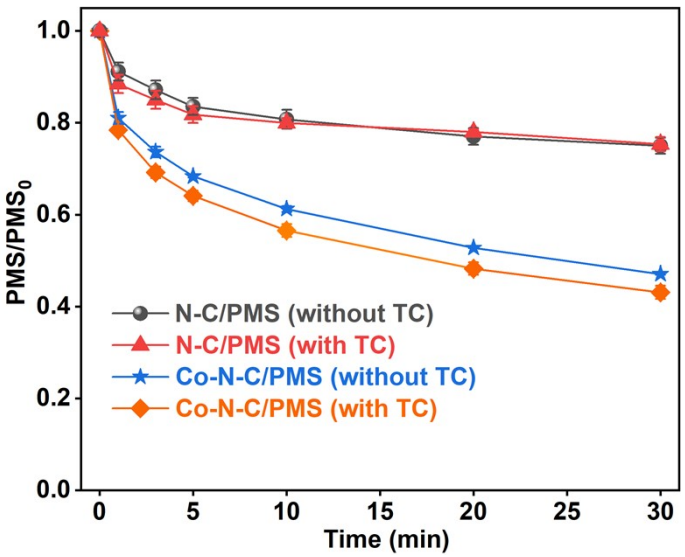

Figure S8. PMS consumption in N-C/PMS and Co-N-C/PMS systems. Experimental conditions: $[TC]_0$ = 10 mg L^{-1}, $[PMS]_0$ = 0.5 mM, $[catalyst]_0$ = 0.15 g L^{-1}, temperature = 25 °C.

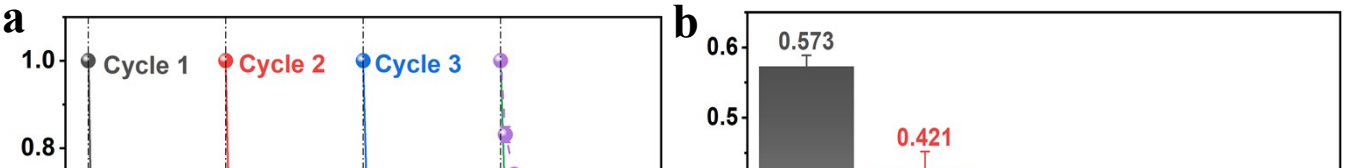

Figure S9. (a) TC degradation and (b) its observed reaction rate of the Co-N-C/PMS system in cycling experiments ($R^2 > 0.9$). Experimental conditions: $[TC]_0$ = 10 mg L^{-1}, $[PMS]_0$ = 0.5 mM, $[catalyst]_0$ = 0.15 g L^{-1}, temperature = 25 °C.

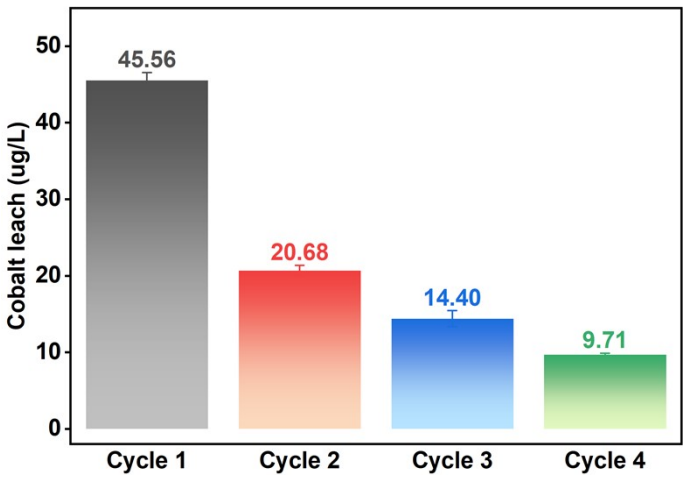

Figure S10. Cobalt leach of the Co-N-C/PMS system in cycling experiments. Experimental conditions: $[TC]_0$ = 10 mg L^{-1}, $[PMS]_0$ = 0.5 mM, $[catalyst]_0$ = 0.15 g L^{-1}, temperature = 25 °C.

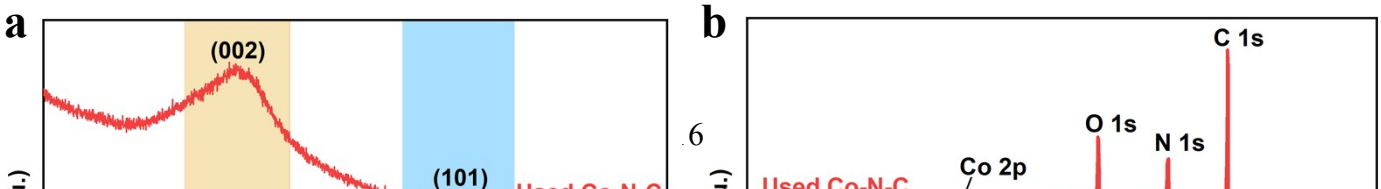

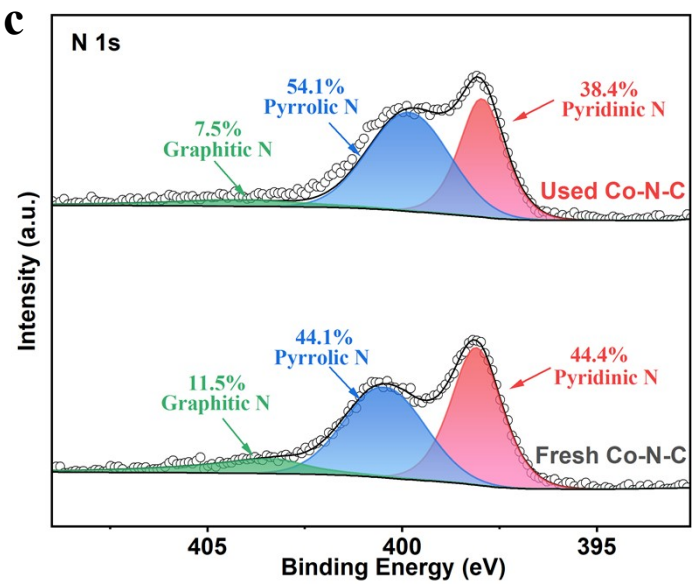

Figure S11. XRD (a) and XPS spectra of fresh and used Co-N-C: (b) survey, (c) N 1s.

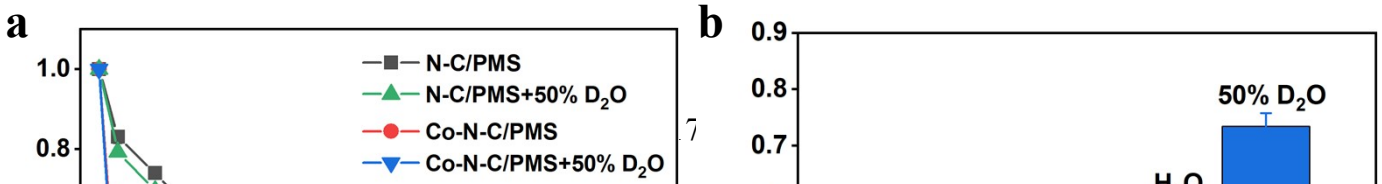

Figure S12. (a) Effect of reaction solvents (H_2O and 50% D_2O) on TC degradation in different systems. (b) Comparison of the rate constant by N-C and Co-N-C (R^2>0.9). Experiment conditions: $[TC]_0$ = 10 mg/L, $[PMS]_0$ = 0.5 mM, $[catalyst]_0$ = 0.15 g/L.

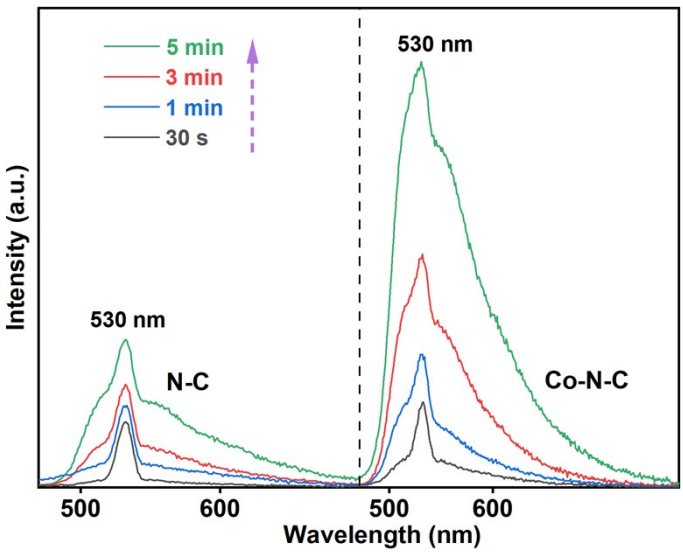

Figure S13. Fluorescence spectra of substrates obtained from $^1O_2$ captured by SOSG in different systems.

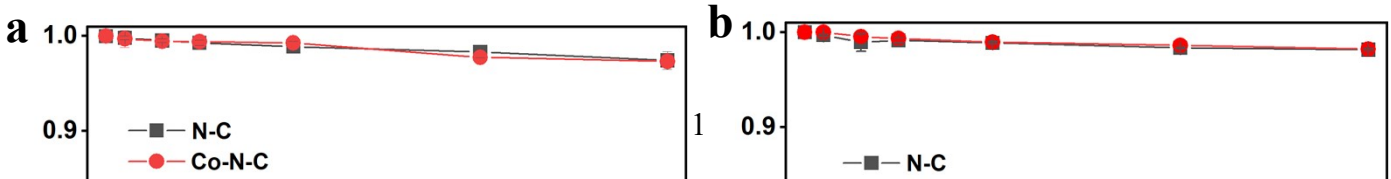

Fig. S14. Degradation of BA (a) and NBT (b) in N-C/PMS and Co-N-C/PMS activated PMS systems. Reaction conditions: $[catalyst]_0 = 0.15$ g L^{-1}, $[PMS]_0 = 0.5$ mM, and $[BA]_0 = [NBT]_0 = 0.1$ mM.

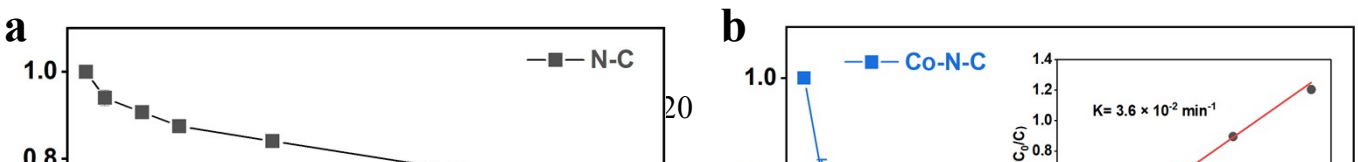

Fig. S15. Loss of FFA in aqueous solution caused by N-C/PMS and Co-N-C/PMS systems (Inset: the corresponding kinetic plot). Reaction conditions: $[catalyst]_0 = 0.15$ g L^{-1}, $[PMS]_0 = 0.5$ mM, and $[FFA]_0 = 0.1$ mM.

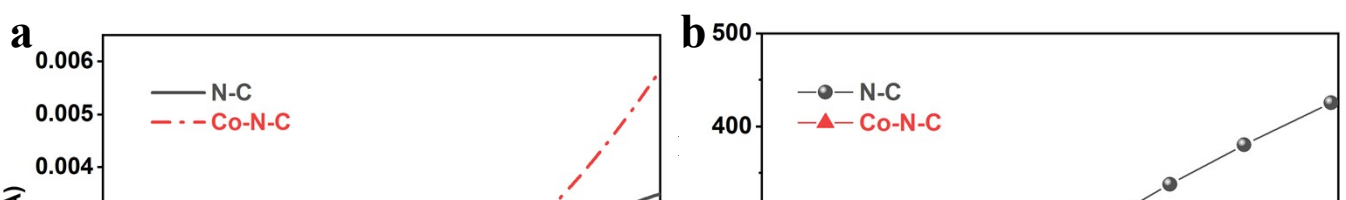

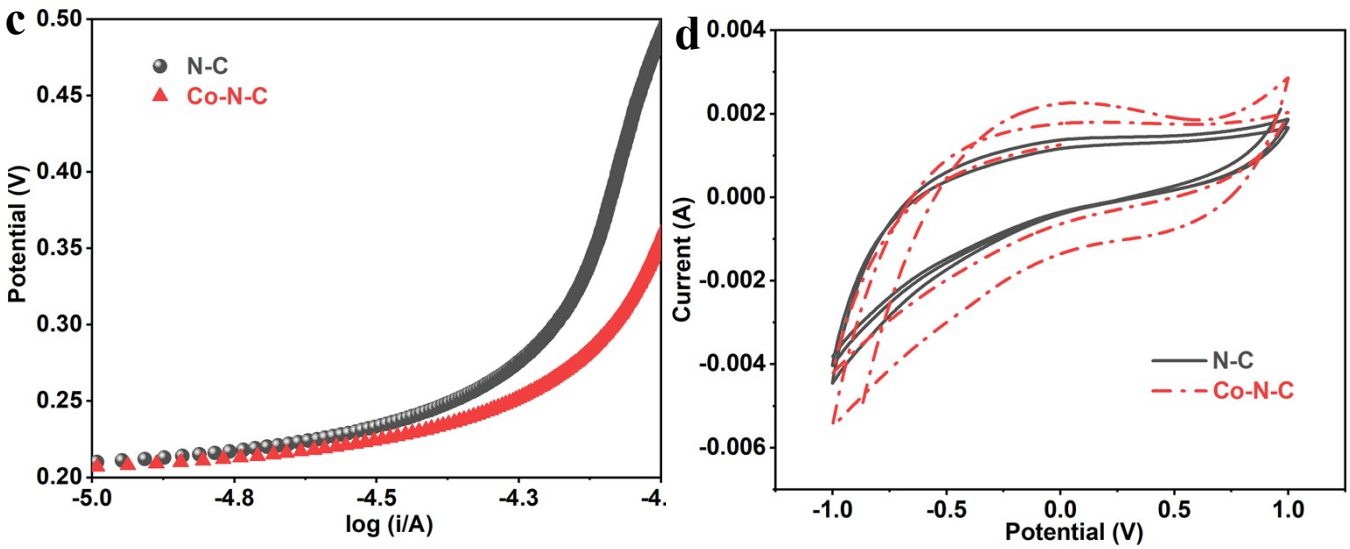

Figure S16. (a) LSV, (b) EIS, (c) Tafel and (d) CV curves of N-C and Co-N-C.

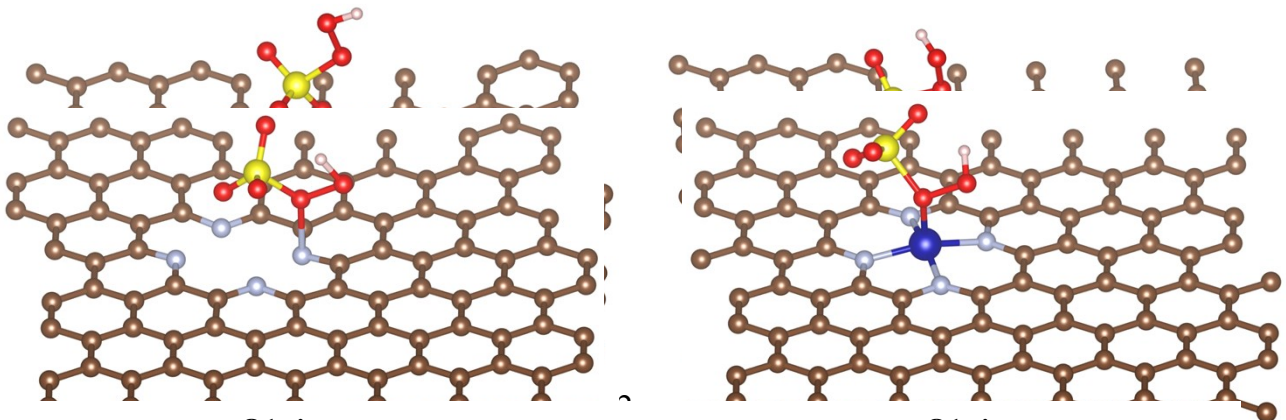

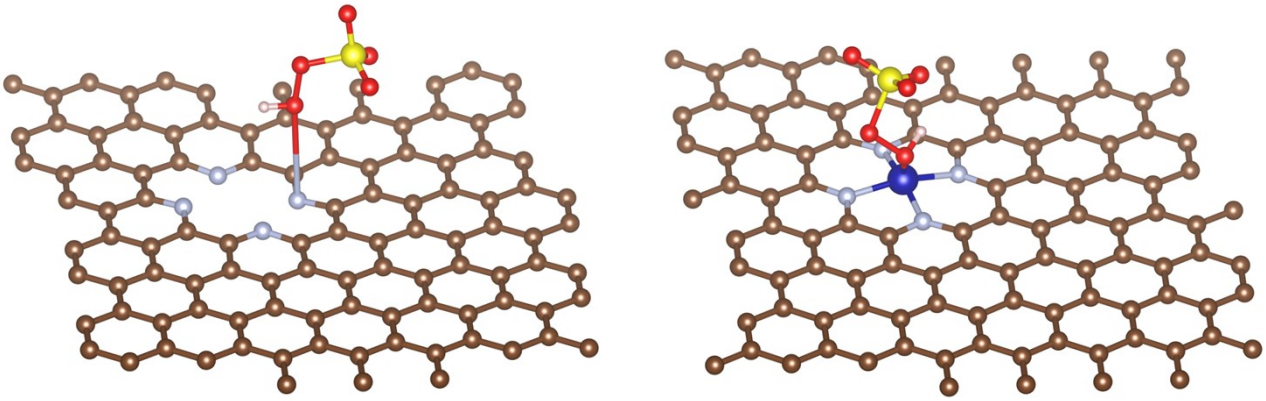

Figure S17. Three local adsorption configurations of PMS on N-C and Co-N-C. (The adsorption energy (E_{ads}) and the length of the O-O bond are indicated below the configuration)

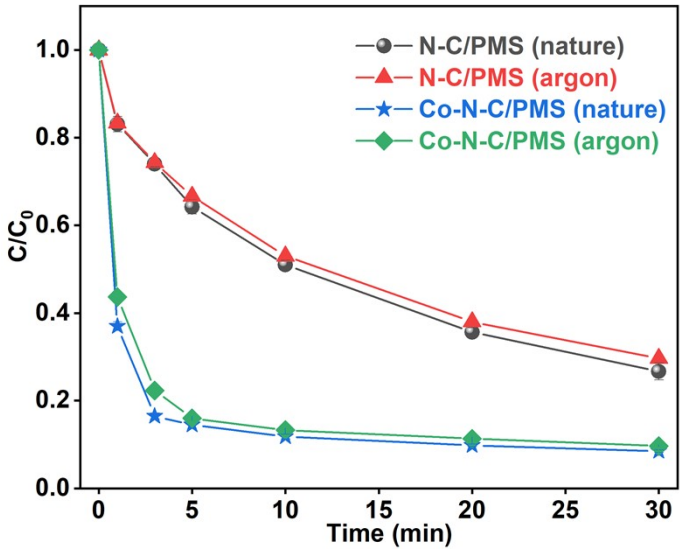

Figure S18. Comparisons of TC degradation by N-C and Co-N-C activated PMS under nature and argon atmospheres. Experimental conditions: $[TC]_0$ = 10 mg L^{-1}, $[PMS]_0$ = 0.5 mM, $[catalyst]_0$ = 0.15 g L^{-1}, temperature = 25 °C, argon = 200 mL min^{-1})

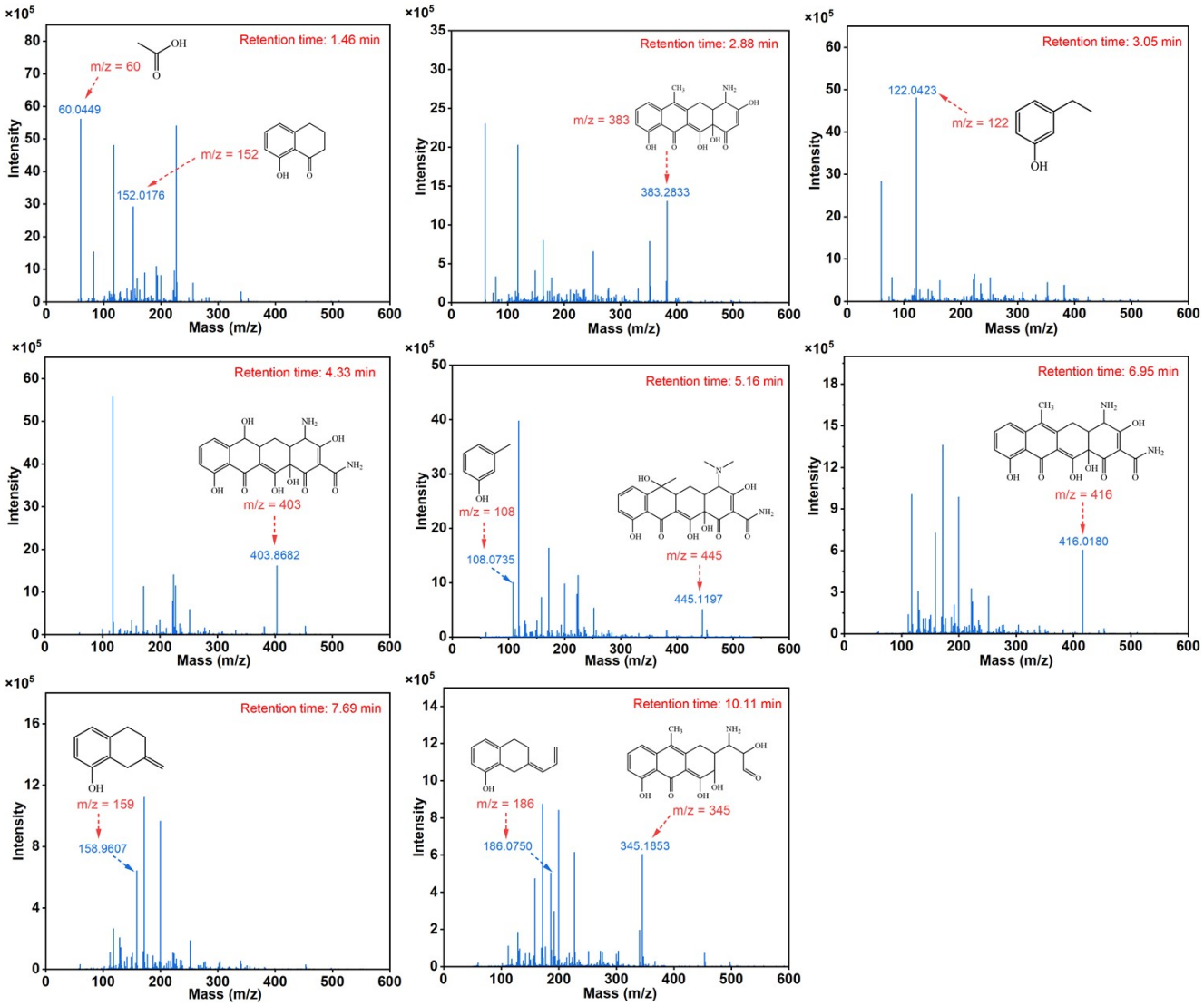

Fig. S19. LC-MS analysis of TC intermediates in the Co-N-C/PMS system at a reaction time of 5 min.

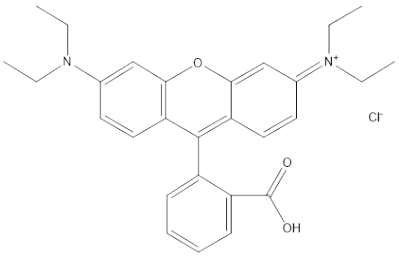

RhB: $C_{28}H_{31}ClN_2O_3$

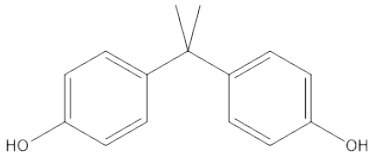

BPA: $C_{15}H_{16}O_2$

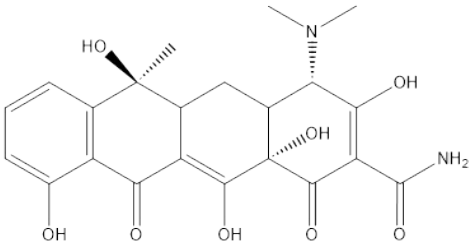

TC: $C_{22}H_{24}N_2O_8$

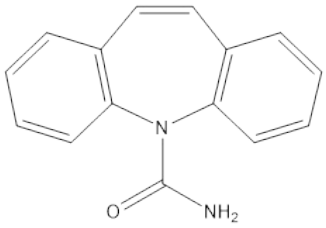

CBZ: $C_{15}H_{12}N_2O$

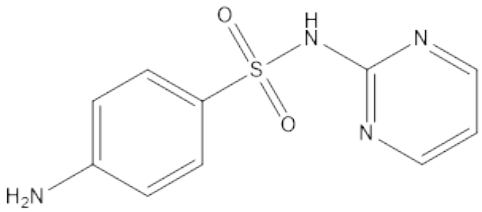

SDZ: $C_{10}H_{10}N_4O_2S$

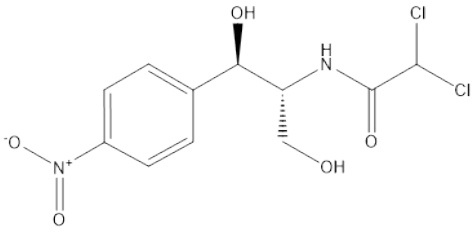

CAP: $C_{11}H_{12}Cl_2N_2O_5$

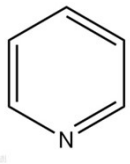

Pyridine: C_5H_5N

Figure S20. Structural formulas of RhB, BPA, TC, CBZ, SDZ, CAP and Pyridine.

RhB is an organic molecule containing a rhodamine core structure, with its molecular structure comprising benzene rings and nitrogen heterocycles. These structural units together form a cyanine core structure, which enables the existence of a large number of π electron clouds within the RhB molecule to form a conjugated system, enhancing the electron density of the molecule, thus exhibiting the electron-rich property. BPA and TC are classified as electron-rich organic compounds because they have electron-donating groups (-OH and -NH_2) attached to their benzene ring skeletons. From the perspective of electron clouds, the benzene ring is a relatively stable structure with a uniform distribution of electron clouds within it. The electron-donating groups attached to the benzene ring possess lone pairs of electrons, increasing the electron cloud density of the benzene ring through conjugative effect. CBZ and SDZ are electron-deficient organic compounds because the nitrogen atom embedded within the benzene ring results in a pyridine-like structure in their

benzene ring skeletons. Pyridine is a typical electron-deficient structure. The pyridine ring is a planar ring with a closed conjugated system within the molecule. Due to the higher electronegativity of the embedded nitrogen atom compared to the carbon atom, the electron cloud density on the pyridine ring is lower than that on the benzene ring. High electron cloud density surrounds the nitrogen atom, while the electron cloud density in other parts of the ring decreases, especially significantly at the ortho and para positions. For CAP, due to the presence of chlorine and nitrogen atoms, which attract surrounding electron clouds, the carbon atoms in the carbon skeleton are placed in a relatively electron-deficient state.

Supplementary Tables

Table S1. HPLC analysis conditions for different organics.

Substrate	Flow (mL/min)	Wavelength (nm)	CH_3OH (%)	H_2O (%)	*EA (%)	Acetonitrile (%)
BPA	0.5	278	70	30	-	-
CAP	0.7	278	40	60	-	-
CBZ	0.7	286	50	50	-	-
SDZ	0.7	270	-	-	70	30

*EA: Eluent A, 0.1% CH_3COOH solution.

Table S2. BET analysis of N-C and Co-N-C.

Sample	BET Surface Area (m^2/g)	Total pore volume (cm^3/g)	Average pore diameter (nm)
N-C	203.63	0.9554	18.77
Co-N-C	187.68	0.7281	15.52

Table S3. EXAFS fitting parameters at the Co K-edge for Co-N-C.

Sample	Path	*CN	†R(Å)	‡σ^2 (Å^2)	§ΔE_0 (eV)	R factor
Co K-edge (S_0^2=0.872)						
Co foil	Co-Co	#12	2.490±0.002	0.0059	6.3	0.0010
Co-N-C	Co-N	4.3±0.6	1.956±0.013	0.0134	-6.0	0.0057

*CN, coordination number; †R, the distance between absorber and backscatter atoms; ‡σ^2, the Debye Waller factor value; §ΔE_0, inner potential correction to account for the difference in the inner potential between the sample and the reference compound; R factor indicates the goodness of the fit. S_0^2 was fixed to 0.872, according to the experimental EXAFS fit of Co foil by fixing CN as the known crystallographic value. # This value was fixed during EXAFS fitting, based on the known structure of Co. Fitting conditions: k range: 2.0 - 10.0; R range: 1.1-2.5; fitting space: R space; k-weight = 3. A reasonable range of EXAFS fitting parameters: $0.800 < S_0^2 < 1.000$; $CN > 0$; $\sigma^2 > 0$ Å^2; $|\Delta E_0| < 10$ eV; R factor < 0.02.

Table S4. Catalytic activity comparison of Co-N-C with currently reported various catalysts in PMS-mediated Fenton-like reactions for TC degradation.

Catalyst (g/L)	PMS dosage (mM)	TC (mg/L)	k_{obs} (min^{-1})	Ref.
Co-N-C (0.15)	0.5	10	**0.573**	**This work**
B-NPC (0.013)	0.217	20	**0.057**	[15]
Co-N/KC-900 (0.16)	1	20	**0.278**	[16]
$CoMn_2O_4$ (0.2)	0.2	22.22	**0.212**	[17]
FCTO-0.15 (0.1)	1	20	**0.0986**	[18]
Fe-PSMPC (0.02)	0.325	20	**0.098**	[19]
NC-Fe_2O_3 (III) (0.2)	0.65	20	**0.158**	[20]
MM3 (0.2)	1	10	**0.150**	[21]
0.1G-MoS_2 (0.05)	1	30	**0.0631**	[22]
Fe_3O_4@PANI-p600 (0.4)	4	20	**0.0353**	[23]
Fe1/ND (0.06)	1	15	**0.283**	[24]

Table S5. Element content of fresh and used Co-N-C.

Sample	C (at%)	N (at%)	O (at%)	Co (at%)
Fresh Co-N-C	75.83	19.80	4.23	0.13
Used Co-N-C	73.97	14.67	11.04	0.11

References

1 Y. Wang, X. Zhao, D. Cao, Y. Wang and Y. Zhu, *Appl. Catal. B-Environ*, 2017, **211**, 79-88.
2 E. T. Yun, J. H. Lee, J. Kim, H. D. Park and J. Lee, *Environ. Sci. Technol.*, 2018, **52**, 7032-7042.
3 Q. Y. Wu, Z. W. Yang, Z. W. Wang and W. L. Wang, *PNAS*, 2023, **120**, e2219923120.
4 P. Neta, V. Madhavan, H. Zemel and R. W. Fessenden, *J. Am. Chem. Soc.*, 1977, **99**, 163-164.
5 G. V. Buxton, C. L. Greenstock, W. P. Helman and A. B. Ross, *J. Phys. Chem. Ref. Data*, 1988, **17**, 513-886.
6 Z. Weng, Y. Lin, S. Guo, X. Zhang, Q. Guo, Y. Luo, X. Ou, J. Ma, Y. Zhou, J. Jiang and B. Han, *Angew. Chem. Int. Ed.*, 2023, **62**, e202310934.
7 Y. Z. Huang, K. Zhu, Z. F. Hu, Y. W. Chen, X. Li, Z. W. Jiang, M. Sillanpää, J. Zhao, R. L. Qiu and K. Yan, *J. Hazard. Mater.*, 2024, **466**, 133611.
8 C. Cheng, S. Gao, J. Zhu, G. Wang, L. Wang and X. Xia, *Chem. Eng. J.*, 2020, **384**, 123377.
9 S. I. Zabinsky, J. J. Rehr, A. L. Ankudinov, R. C. Albers and M. j. Eller, *Physical Review. B. Condensed Matter*, 1995, **52**, 2995−3009.
10 B. Ravel and M. Newville, *J. Synchrotron Radiat.*, 2005, **12**, 537-541.
11 G. Kresse and D. Joubert, *Physical Review B*, 1999, **59**, 1758-1775.
12 P. E. Blochl, *Phys Rev B Condens Matter*, 1994, **50**, 17953-17979.
13 J. P. Perdew, K. Burke and M. Ernzerhof, *Phys. Rev. Lett.*, 1996, **77**, 3865-3868.
14 J. P. Perdew, M. Ernzerhof and K. Burke, *J. Chem. Phys.*, 1996, **105**, 9982-9985.
15 J. Xie, X. Luo, L. Chen, X. Gong, L. Zhang and J. Tian, *Chem. Eng. J.*, 2022, **440**, 135760.
16 H. Zhu, A. Guo, S. M. Wang, Y. Long, G. Y. Fan and X. J. Yu, *Chem. Eng. J.*, 2022, **450**, 138428.
17 T. B. Nguyen, C. P. Huang, R. Y. Doong, M. H. Wang, C. W. Chen and C. D. Dong, *Chem. Eng. J.*, 2022, **436**, 135244.
18 J. Wei, D. Han, J. Bi and J. Gong, *Chem. Eng. J.*, 2021, **423**, 130165.
19 M. Yang, W. Wang, H. Ma, X. Lu, L. Chen, Y. Li and H. Ma, *Chem. Eng. J.*, 2024, **479**, 147882.
20 M. Wang, S. Li, J. Kang, Y. Tang, J. Wang, Z. Xu and J. Liu, *Chem. Eng. J.*, 2023, **451**, 138611.
21 P. Xu, S. Xie, X. Liu, L. Wang, R. Wu and B. Hou, *Chem. Eng. J.*, 2024, **480**, 148233.
22 X. Li, L. Wang, Y. Guo, W. Song, Y. Li and L. Yan, *Chem. Eng. J.*, 2022, **450**, 138104.
23 Y. Wang, K. Li, M. Shang, Y. Zhang, Y. Zhang, B. Li, Y. Kan, X. Cao and J. Zhang, *Chem. Eng. J.*, 2023, **451**, 138655.
24 M. Yang, K. Wu, S. Sun, J. Duan, X. Liu, J. Cui, S. Liang and Y. Ren, *ACS Catal.*, 2023, **13**, 681-691.